Radiation Physics and Chemistry 155 (2019) 164–172

Contents lists available at ScienceDirect

Radiation Physics and Chemistry

journal homepage: www.elsevier.com/locate/radphyschem

# Wearable detector device utilizing microstructured semiconductor neutron detector technology

T.R. Ochs[a,*], B.L. Beatty[b], S.L. Bellinger[c], R.G. Fronk[a], J.A. Gardner[b], L.C. Henson[c], D.E. Huddleston[d], R.M. Hutchins[a], T.J. Sobering[d], J.L. Thompson[b], A. Van Bergeijk[a], D.S. McGregor[a]

[a] Semiconductor Materials and Radiological Technologies (S.M.A.R.T.) Laboratory, Department of Mechanical and Nuclear Engineering, Kansas State University, Manhattan, KS 66506, USA
[b] Alion Science and Technologies Corp., McLean, VA 22012, USA
[c] Radiation Detection Technologies, Inc., Manhattan, KS 66502, USA
[d] Electronics Design Laboratory, Kansas State University, Manhattan, KS 66506, USA

ARTICLE INFO

*Keywords:*
Microstructured Semiconductor Neutron Detector (MSND)
Neutron detector
Wearable detector
Solid-state detector
Helium-3 replacement

ABSTRACT

A Wearable Detector Device (WDD) has been outfitted with Microstructured Semiconductor Neutron Detectors (MSNDs) to aid in the search and localization of special nuclear materials (SNMs). Many SNMs decay by spontaneous fission and emit free neutrons. The WDD detects these neutrons and stores interaction rate information to alert the operator to the presence of special nuclear material. The WDD is composed of 16 Modular Neutron Detectors (MNDs), each populated with a 4 × 6 array of 1-cm$^2$ active area, 500-μm thick MSNDs. The individual MSNDs each have an intrinsic thermal-neutron detection efficiency of approximately 30%. Each MND connects to a communications dongle, and the MND and dongle were encased in a 3-in. wide by 5-in. tall by 0.6-in. thick high-density polyethylene moderator (HDPE) case. The 16 MNDs, connected to Controller Area Network dongles, communicate with a master control board, which also contains the battery bank and power conditioning electronics. The operational lifetime of the battery-powered WDD is greater than 12 h per single charge. The WDD, mounted on an ANSI 42.53 phantom, reported 8.12 ± 0.07 cps and 12.93 ± 0.07 cps for a bare and moderated 21.9-ng $^{252}$Cf source at a distance of 1 m, respectively. The background count rate was 0.446 ± 0.002 cps. The gamma-ray rejection ratio of the WDD for $^{137}$Cs measured at a dose rate of 10 mR/h was $1.8 \times 10^{-8}$.

## 1. Introduction

The increased importance of nuclear non-proliferation efforts has motivated research into advanced radiation sensors that can be used to detect the presence of Special Nuclear Material (SNM). Most SNM decays by spontaneous fission, which results in the emission of both gamma rays and neutrons. SNMs can therefore be detected by measuring the emitted gamma rays, emitted neutrons, or both. Unfortunately, many isotopes that may not be the SNM of interest also emit gamma rays, including: radiotracers, soil-density gauge sources, and many radioisotopes used for medical procedures. Additionally, background gamma-ray radiation levels can vary widely over relatively small areas depending on the type of terrain and elevation (Aucott et al., 2013; Mitchell et al., 2011). Therefore, relying solely on gamma-ray detection for the search and localization of SNMs may be unreliable. Utilizing neutron detection for search and localization of SNM is advantageous, because only a limited number of isotopes emit neutrons most of which would be classified as SNM. Furthermore, background neutron radiation levels tend to be low (Gordon et al., 2004), and thus, detection of free neutrons above the background radiation level would alert an operator that further interrogation is required.

Historically, $^3$He gas-filled proportional counters have been consider the "gold standard" for thermal-neutron detection. $^3$He has a large thermal-neutron absorption cross section and the corresponding reaction products have sufficient energy to produce an electronic pulse well above the background noise and gamma-ray response of the detector. However, a shortage of $^3$He gas, appearing during the post-nuclear weapon production era, has caused the price of $^3$He gas to significantly increase, making $^3$He detectors expensive to fabricate. Therefore, there has been an effort in recent years to develop alternative thermal-

* Correspondence to: 3002 Rathbone Hall, 1701B Platt St., Manhattan, KS 66506, USA.
*E-mail address:* trochs@ksu.edu (T.R. Ochs).

https://doi.org/10.1016/j.radphyschem.2018.08.028
Received 31 July 2017; Received in revised form 20 August 2018; Accepted 23 August 2018
Available online 23 August 2018
0969-806X/ 

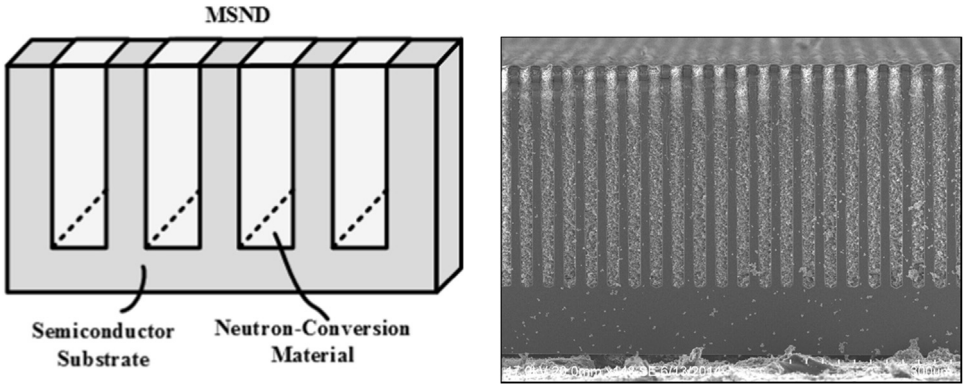


**Fig. 1.** Schematic (left) and SEM image (right) of MSND backfilled with $^{6}$LiF powder. The trenches are approximately 20-μm wide and 400-μm deep with silicon fin widths of 10 μm.

neutron detectors that do not utilize $^{3}$He as a detection medium.

Microstructured Semiconductor Neutron Detectors (MSNDs) are one such $^{3}$He-replacement technology that was developed over the past decade as an affordable, durable, and reliable solution for thermal-neutron detection (Bellinger et al., 2013; McGregor et al., 2015, 2013, 2009, 2008; Nikolic et al., 2007; Nikolić et al., 2008; Ochs et al., 2014; Shultis and McGregor, 2009; Uher et al., 2007). MSNDs operate as a *pιn*-junction diode with microfeatures etched into a semiconductor substrate that are subsequently backfilled with neutron conversion material, see Fig. 1. Upon absorption of a neutron, the neutron conversion material fissions into two charged-particle reaction products. When the reaction products traverse through the semiconductor substrate, they create electron-hole pairs through Columbic interactions. The electrons and holes are drifted towards their respective contacts through the influence of an applied bias, and the charge motion in the semiconductor induces current in the detection circuitry to form an electronic charge pulse. MSNDs with straight trenches backfilled with $^{6}$LiF are theoretically capable of intrinsic thermal-neutron detection efficiencies greater than 45% for normally incident neutrons (Shultis and McGregor, 2009).

Several classifications of detector systems have been developed for the detection of SNMs including portal monitors, hand-held counters, backpack detector systems, and recently, wearable detector systems. In addition to utilizing a non-$^{3}$He conversion material, the compact size and low power consumption of the MSND package makes MSNDs an ideal candidate to be utilized in a low-profile wearable detector system capable of overt and covert operation. In this work, a Wearable Detector Device (WDD) was fabricated comprising Modular Neutron Detectors (MNDs) populated with MSNDs, a battery-bank power supply, controller area network (CAN bus) dongles, and a handheld Android Device for user interface.

## 2. Detector fabrication and specifications

The following sections review the present fabrication processes for MSNDs and MSND device characteristics. The specifications for the MND are then discussed, which are integrated into the WDD system.

### 2.1. Microstructured Semiconductor Neutron Detector (MSND)

MSNDs are mass produced using standard VLSI processing techniques at Kansas State University. 1-cm$^{2}$ active area diodes are manufactured on 100-mm diameter, 525-μm thick, (110)-orientated silicon wafers. Photolithography is used to pattern 20-μm wide trenches with 10-μm wide fins into a $SiO_2$ layer grown on the surface of the Si substrate. The patterned oxide then serves as an etch mask during the anisotropic KOH wet-etch where the straight trenches are aligned parallel to the (111)-plane and etched approximately 400-μm deep on one side of the wafer. Next, the wafers are cleaned, and then, solid-source diffusion processes are performed to form *n*-type and *p*-type contacts on the planar and trenched side of the wafer, respectively. A Ti/Au ohmic contact is then evaporated on planar side of the wafer and bond pads on the trenched side. The MSNDs can then be diced and mounted into individual detector packages (Bellinger et al., 2013; Ochs et al., 2014). The MSNDs are operated with 0 V to − 5 V applied bias. The leakage current for 1-cm$^{2}$ MSNDs operated at − 2.7 V applied bias is less than 5 nA cm$^{-2}$, and the capacitance is less than 120 pF cm$^{-2}$ at − 3 V. The leakage current and capacitance were measured with a Keithley Instruments IV-curve-tracing system and a 1-MHz Hewlett-Packard CV-curve-tracing system, respectively. The intrinsic thermal-neutron detection efficiency of the MSND is then determined by calibrating against at 4-atm Reuter-Stokes $^{3}$He gas filled detector with known detection efficiency in a collimated, diffracted, thermal-neutron beam at the Kansas State University TRIGA Mk II nuclear reactor (McGregor and Kenneth Shultis, 2011). The intrinsic detection efficiency for thermal neutrons of the MSNDs used in the WDD were approximately 30% (Radiation Detection Technologies, 2017).

### 2.2. Modular Neutron Detector (MND)

The MND was designed to serve as a low-power, low-profile, modular platform that could be integrated into small, light-weight, hand-held or wearable detector systems. Each MND measures 9.5 cm × 6.0 cm × 0.6 cm and contains twenty-four 1-cm$^{2}$ active-area MSNDs arranged on a 4 × 6 array where four MSNDs compose a channel (see Fig. 2). Every channel on the MND has a dedicated preamplifier, amplifier, and pulse-height discriminator with TTL-pulse generator. The six channels on the MND are then connected to a wired “OR” logic gate. When charge carriers, created from charged-particle interactions in the Si substrate, are drifted toward their respective contacts, a current is induced in the detection circuitry and used to form a voltage pulse. The signal is then amplified in the preamplifier and shaping amplifier before it is passed to the pulse-height discriminator. If the height of the pulse is higher than the lower level discriminator (LLD), a digital square-wave TTL-pulse is generated and sent through the wired “OR” logic gate. The pulses are then accumulated on an 8-bit counter on the MND until the counts are read-out by the attached communications dongle. The MND also includes programmable bias and LLD shared across all the channels. An onboard temperature monitor measures the operating temperature of the MND, which can be used to adjust bias and LLD settings accordingly. Fig. 3 is a block diagram of the MND electronics. The MND was designed to connect to a communications dongle, which then interfaces with the rest of the WDD system. Different communication dongles can be made to fit the end users need whether that be to output through CAN protocol, via a BNC connection, or even wirelessly through Bluetooth. In the WDD, the MNDs are attached to CAN dongles

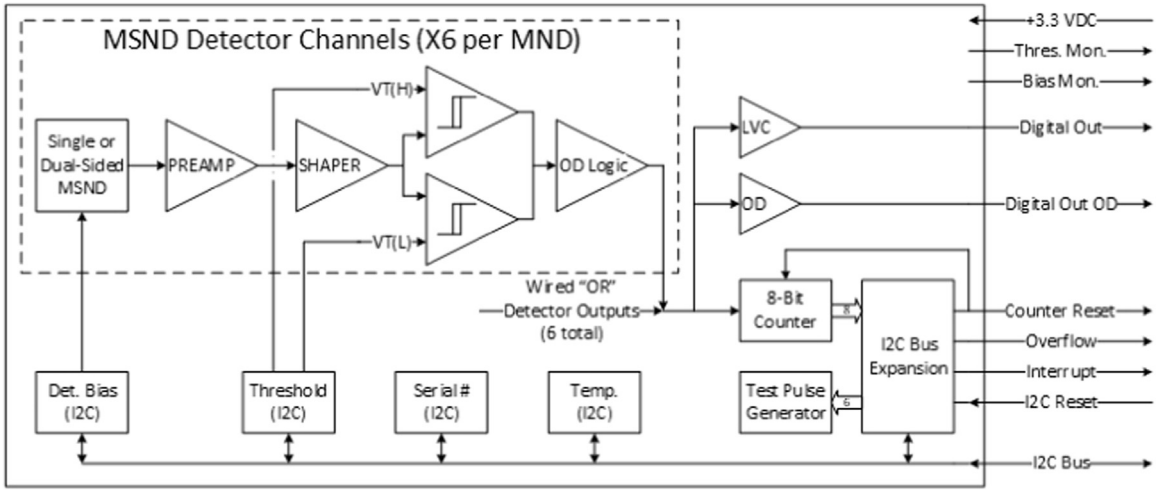


**Fig. 2.** MND schematic showing six channels each containing four MSNDs. Each channel includes a dedicated preamplifier, shaping amplifier, and pulse-height discriminating electronics. A common programmable bias and lower level discriminator is set for each MND. Pulses are stored on an 8-bit counter to be read out through the attached communications dongle.

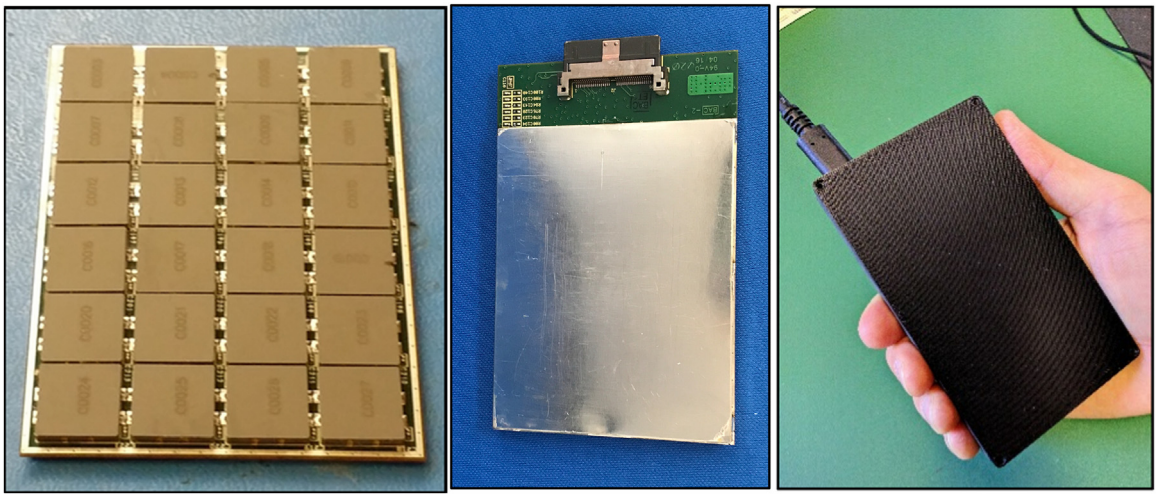

**Fig. 3.** (Left) MND with 24, 1-cm$^2$ MSNDs. There are six channels per MND each containing four MSNDs. (Middle) MND with EM-shield covering the MSNDs. The MND connects to a communications dongle. (Right) MND enclosed a 3-in. × 5-in. × 0.6-in. HDPE moderator case. The case houses both the MND and communications dongle and allows access to the USB Type-C port on communications dongle.

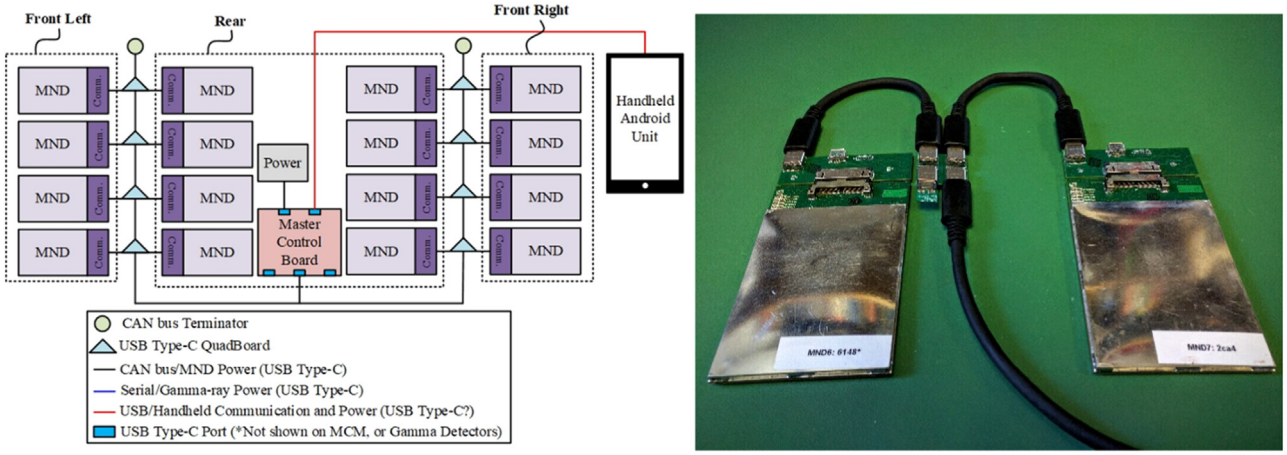


**Fig. 4.** (Left) Layout of fully-populated WDD system. The 16 MNDs connect to CAN communications dongles, which then interface with a master control board. The master control board outputs the neutron count rate to the handheld Android unit every second. (Right) MNDs connected to CAN communications dongles and then connected to a USB Type-C QuadBoard.

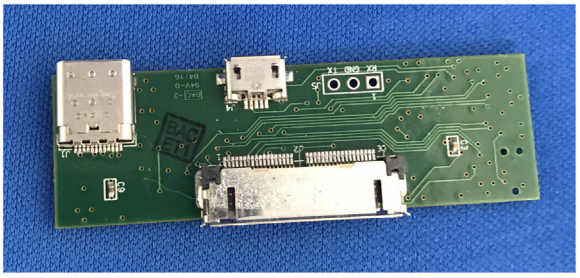

**Fig. 5.** The CAN communication dongle measures 2 cm × 6 cm and connects directly to a MND. The CAN dongle can write threshold and bias settings and reads in count rate data from the MND, which is then sent upstream to the master control board. The CAN dongle is enclosed in the HDPE moderator case with the attached MND.

and both are enclosed in a 12.7-cm × 7.6-cm × 1.5-cm HDPE moderator case. The current draw for a single MND is approximately 4 mA at 3.3-V operating voltage. The intrinsic detection efficiency for a MND in a moderator case for bare $^{252}$Cf was 0.193% ± 0.002%. The efficiency measurement was performed with a bare 21.9-ng $^{252}$Cf source at 50 cm. Each MND was then calibrated to match the count rate of the calibrated MND to within 1% by adjusting the LLD threshold on the remaining 15 MNDs. For comparison the RadEye™ NL Personal Highly Sensitive Radiation Detector, which measures 9.6 cm × 6.1 cm × 3.1 cm and implements a 2.5-bar $^{3}$He detector, is quoted to report 2 cps/mrem/h for $^{252}$Cf when worn on the body ("RadEyeTM NL Personal Highly Sensitive Neutron Radiation Detectors," n.d.). The MND operating in a stand-alone configuration without a body or phantom as moderator reported approximately 1.5 cps/mrem/h for a bare $^{252}$Cf source.

### 2.3. Wearable Detector Device (WDD) system

The WDD system comprises 16 MNDs, 16 CAN communications dongles, 8 USB Type-C Quad-Connector Boards (QuadBoard), a master control board, a battery pack with power regulating electronics, and a handheld Android device, see Fig. 4. Each MND connects directly to a CAN communications dongle, and the CAN dongles connect QuadBoards that are then attached the master control board via USB Type-C cables. The CAN dongle can read the total counts accumulated by the six channels of MSNDs on the MND every 0.1–1 s. The CAN dongle (Fig. 5.) then sends the count rate information upstream to the master control board. The master control board pushes the total number of counts from each MND to the handheld Android unit once per second, and the real-time count rate and gross counts accumulated are displayed on the Android application, see Fig. 6. Real-time count rate information for individual MNDs can also be monitored on the Android application. The fully-populated WDD draws approximately 300-mA current at 3.3 V, and the battery pack attached to the master control board contains three 3400-mAh rechargeable batteries. Thus, over 12 h of continuous operation is possible on a single battery charge. The entire WDD system with 16 MNDs, 16 CAN dongles, and a master control board with batteries weighs 12 pounds (5.44 kg), and the populated prototype garment is shown in Fig. 7.

## 3. WDD sensitivity measurements, experimental methods

The WDD was secured on an acrylic phantom with dimensions described in ANSI 42.53 for all radiation measurements performed (Fig. 8). The phantom simulates the neutron moderating effects of a person wearing the WDD during operation. The center of the WDD was 1-m above the floor and the source-to-detector distance was measured from the front of the WDD to the center of the source. All measurements were performed with the source 1-m above the floor. The WDD response to a bare, 21.9-ng $^{252}$Cf source was measured for source-to-detector distances of 0.5, 1.0, 1.5, and 2.0 m. The measurements were

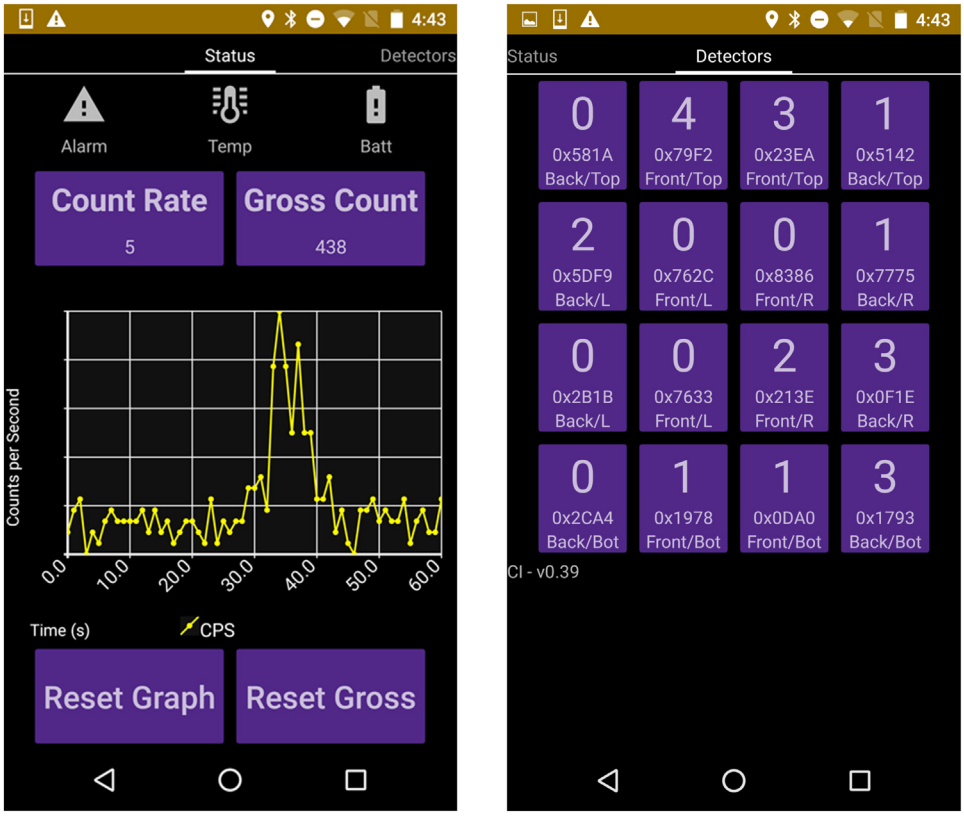


**Fig. 6.** (Left) Android Application GUI. The real-time count rate and total gross counts are displayed on the "Status" screen along with a plot of the count rate for the most recent 60 s. An operator approached and then walked away from a stationary neutron source in the plot displayed in the picture. (Right) The count rates for individual MNDs can be monitored on the "Detectors" screen of the Android interface software.

**Fig. 7.** WDD system installed in discrete prototype garment. The WDD offers a low-profile, low-power, light-weight, high efficiency means for neutron detection.

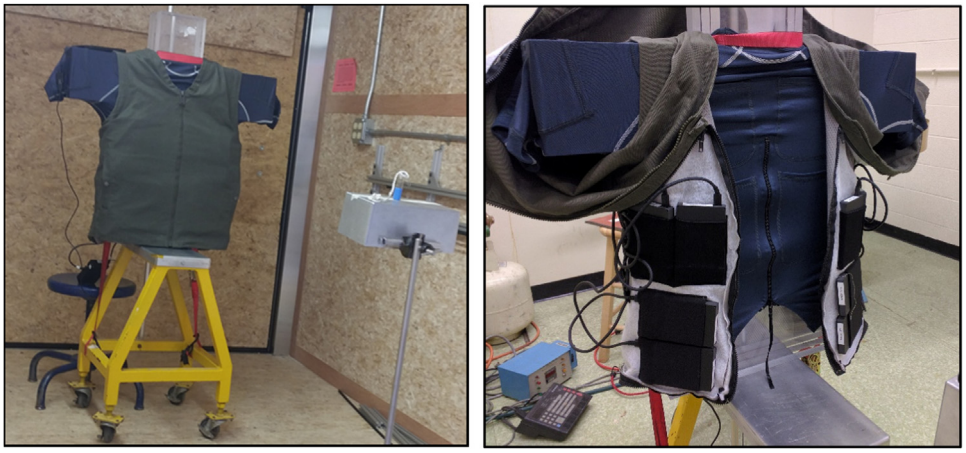

**Fig. 8.** WDD fitted on ANSI42.53 acrylic phantom for neutron and gamma-ray sensitivity measurements. The center of the WDD was 1-m above the floor.

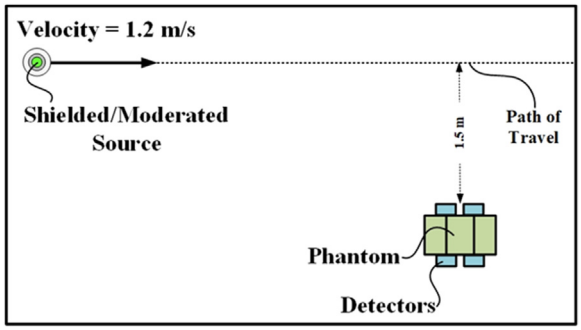


**Fig. 9.** Moving source measurements diagram. The experiment depicted was for moderated $^{252}$Cf traveling at 1.2 m/s with a distance of closest approach of 1.5 m.

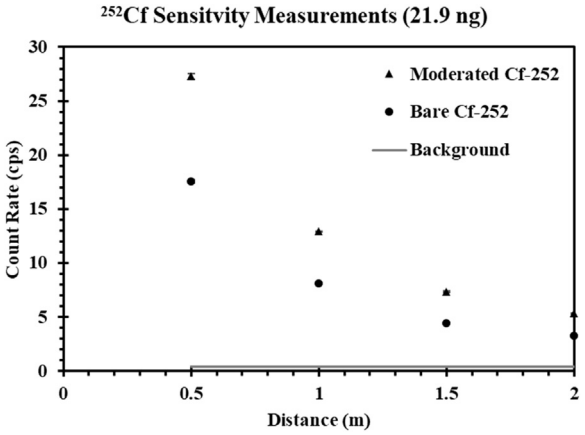


**Fig. 10.** WDD response to a bare and moderated $^{252}$Cf with a mass of 21.9 ng as a function of source-to-detector distance. Note that the error bars are smaller than the data point icon.

then repeated with the $^{252}$Cf source placed inside a 9.7-cm diameter by 12.8-cm tall moderator cask composed of 0.5-cm thick lead, 1-cm thick steel, and 2.5-cm thick HDPE concentric cylinders. Next, measurements were performed with a bare AmBe source at 0.5, 1.0, 1.5, and 2.0 m. The emission rate of the AmBe source was approximately 213,000 neutrons per second. The angular dependence of the WDD was measured with a moderated $^{252}$Cf source at 1.5 m, and the WDD was rotated through 360 ° in 45 ° increments. A 1-mCi $^{137}$Cs was used to determine the WDD system's gamma-ray rejection ratio at a dose rate of 10-mR/h. Moving source measurements were also performed with bare and moderated $^{252}$Cf at a source-to-detector distance of 1.5 and 1 m at the point of closest approach, see Fig. 9. The source was moved at speeds of 1.2 m/s and 0.6 m/s. Borated HDPE shields 5-cm thick were placed at the starting and ending locations of the track, and the source was in the line-of-sight to the WDD for 2.9-m of the track.

## 4. Results and discussion

A plot of the WDD count rate vs. source-to-detector distance for a bare and moderated 21.9-ng $^{252}$Cf source is displayed in Fig. 10, and the response to a bare AmBe source is shown in Fig. 11. The neutron count rate decreases as the source-to-detector distance increases due to the

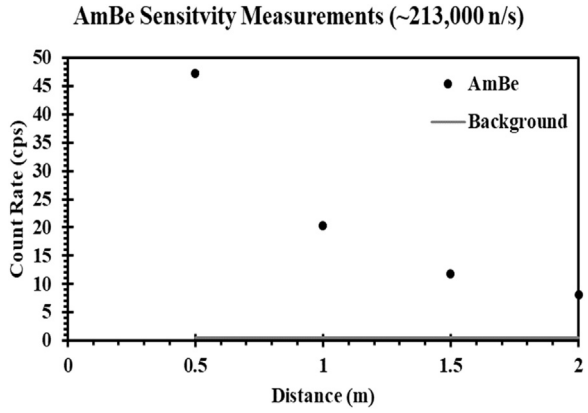


**Fig. 11.** WDD response to a bare AmBe source emitting approximately 213,000 n/s as a function of source-to-detector distance. Note that the error bars are smaller than the data point icon.

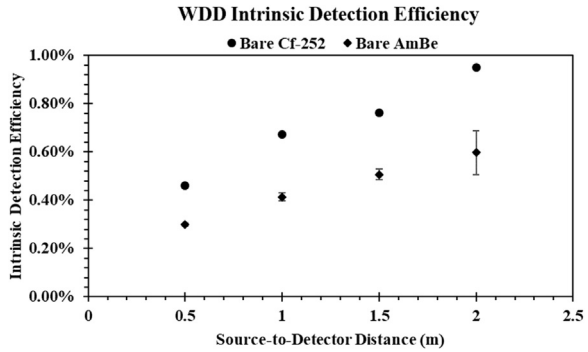


**Fig. 12.** Intrinsic neutron-detection efficiency for a bare $^{252}$Cf and bare AmBe source. The entire forward-facing area of the phantom was considered the detector window for the solid-angle corrections. An increase in intrinsic neutron-detection efficiency as distance increases was likely due to parallax effects and a decreased average neutron energy.

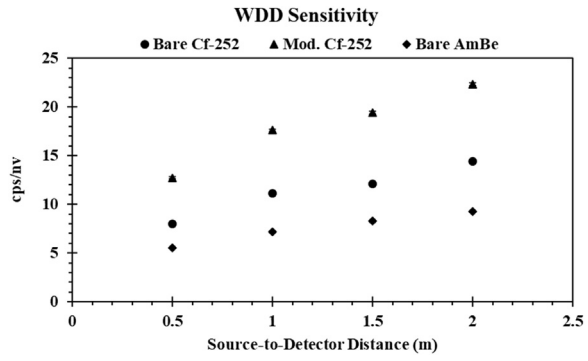


**Fig. 13.** WDD sensitivity in cps/nv as a function of source distance. The flux at the location of the detectors was determined by MCNP6 simulations by calculating the average flux in the phantom volume at each source location. Note that the error bars are smaller than the data point icon.

decreased detector solid angle, but at all positions the count rate with the source present is significantly higher than the background count rate of 0.446 ± 0.002 cps.

The intrinsic neutron-detection efficiency of a detector is determined by dividing the measured net count rate by the number of neutrons that intersect the detector entrance window per unit time. To determine the rate at which neutrons pass through the detector window, one can multiply the source emission rate by the fractional solid angle of the detector as seen by the source. The area of the face of the detector being irradiated is used to calculate the fractional solid angle, but this analysis becomes more complicated for a system utilizing multiple detectors, especially when the detectors are arranged around a moderator such as the phantom. One could argue that any neutron that intersects the phantom has a chance of being scattered into a detector worn on the phantom. Therefore, the entire surface area of the phantom with dimensions described in ANSI 42.53 was used for the "detector window" in the solid-angle calculation and is being adopted as the standardized method of reporting intrinsic neutron-detection efficiency for wearable detector systems containing detectors of different shapes, sizes, and configurations.

The WDD intrinsic detection efficiency for bare $^{252}$Cf and bare AmBe versus source-to-detector distance is shown in Fig. 12. Intuitively, one would argue that the intrinsic detection efficiency should be constant regardless of source distance, but an increase in intrinsic detection efficiency was observed as the source distance increased. Two phenomena likely attribute to this observation. First, parallax effects would be more pronounced at short source-to-detector distances, where neutrons can have very short path lengths inside the detectors or phantom near the edges. Degradation from parallax would decrease as the source is moved further from the detector. Second, the average energy of the neutrons intersecting the WDD will decrease as the source distance is increased, due to neutrons scattering within the environment. The WDD uses $^{6}$LiF as the conversion material, which has a cross section proportional to $1/v$ in the thermal energy range where $v$ is the velocity of the neutron, and thus, would have a higher probability of detecting these lower energy neutrons. This effect is also observed by noting that the WDD sensitivity is highest for moderated $^{252}$Cf, followed by bare $^{252}$Cf, and then bare AmBe. Perhaps a more useful way to report the WDD sensitivity would be the expected count rate of the system if the WDD was in a uniform neutron flux environment, which would have the commonly reported unit of counts per second per unit neutron flux (cps/nv) as shown Fig. 13. The flux at the location of the detector was determined by tallying the average flux inside the phantom volume through MCNP6 modeling. Again, the sensitivity increases as the source-to-detector distance increases.

The relative angular response of the WDD to a moderated $^{252}$Cf source at 1.5 m is shown in Fig. 14 and normalized to the normally incident, 0 °, position. When the WDD was irradiated at 90° and 270°, the count rate decreased to approximately 60% of the normally-incident neutron count rate. The count rate depression stems from a large decrease in solid angle between the source and phantom. The gamma-ray rejection ratio was measured as $1.8 \times 10^{-8}$ for $^{137}$Cs at a dose rate of 10 mR/h demonstrating low gamma-ray sensitivity.

The results of the moving source measurements are show in Figs. 15–18. The background count rate with the source behind the borated-HDPE shields at the starting and ending locations was 1.94 ± 0.06 cps and 2.70 ± 0.06 cps, respectively. The higher than previously reported background count rate was due to neutrons streaming through the borated HDPE sheets, thereby, artificially increasing neutron background levels. For each measurement, the WDD started logging data at the 30-s mark, and the source started moving across the track at the near 70-s mark. The signal for the bare $^{252}$Cf source at 1.5-m moving at the 1.2 m/s blends in with the elevated background levels, but prominent count rate spikes above the background signal were observed for the bare $^{252}$Cf source moving 0.6 m/s and the moderated $^{252}$Cf source at both speeds. A more time-resolved plot could be achieved if the count rate data was reported to the Android device at a faster rate than once per second, but the adjustment would also increase the power consumption of the system. This tradeoff may be beneficial depending on the mission requirements. An alarm window could also be implemented where counts are integrated over a set time regardless of the count rate data acquisition speed, and if the number of counts recorded during this time interval is higher than the expected count rate from background radiation over the same time interval, an alarm would be triggered. The required length of the alarm

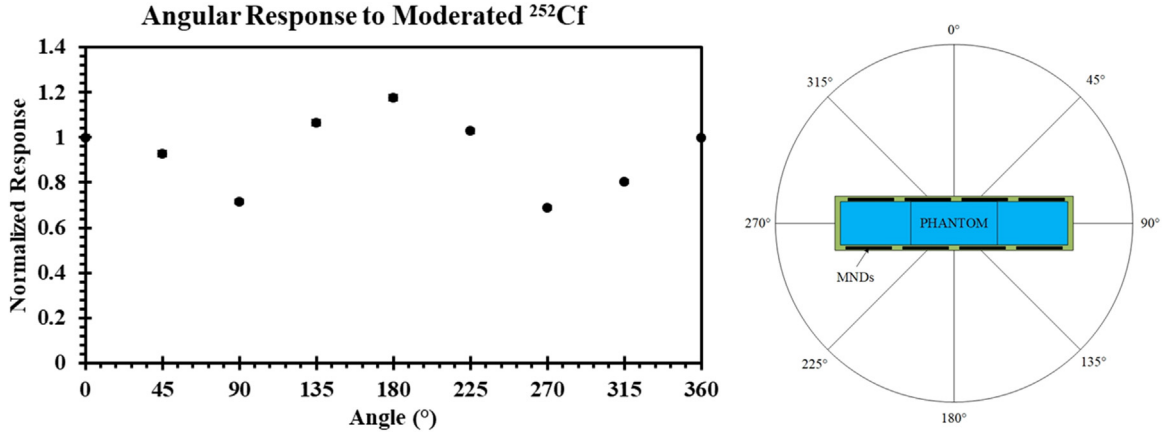


**Fig. 14.** Relative angular response of the WDD to a moderated $^{252}$Cf source at 1.5 m. Note that the error bars are smaller than the data point icon.

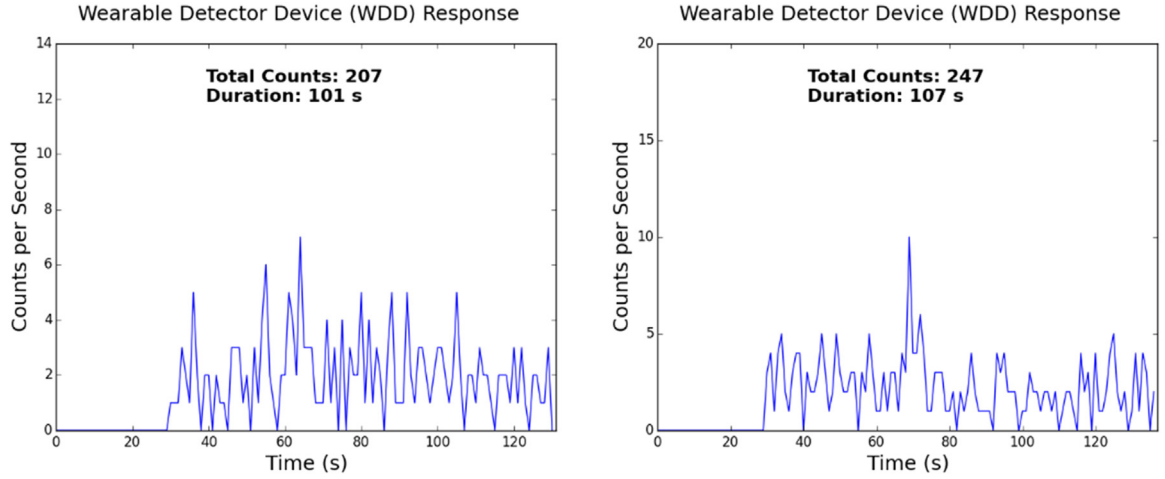


**Fig. 15.** Moving source measurements for bare $^{252}$Cf with the WDD 1.5 m from the source at closest approach. The source was moving at approximately 1.2 m/s in the left plot and 0.6 m/s in the plot on the right.

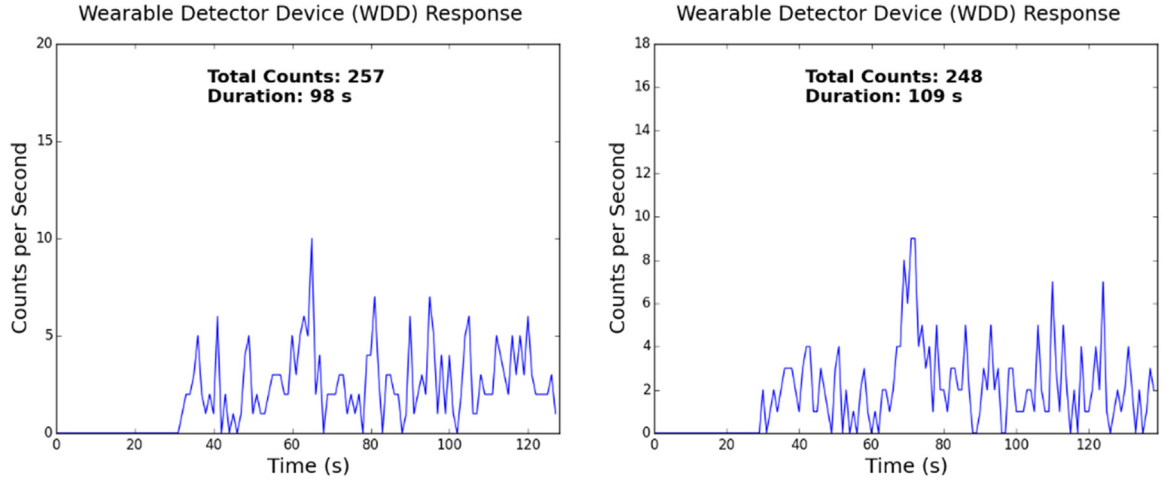


**Fig. 16.** Moving source measurements for moderated $^{252}$Cf with the WDD 1.5 m from the source at closest approach. The source was moving at approximately 1.2 m/s in the left plot and 0.6 m/s in the plot on the right.

window would depend the detector noise and sensitivity to neutrons. A high-sensitivity, low-noise detector could operate with a shorter alarm window than a detector with lower sensitivity and higher background noise level. If an alarm was triggered, the data collected during the alarm window could be investigated further. When the distance of closest approach was reduced to 1-m, the time of closest approach could be identified for both moderated and bare $^{252}$Cf at both speeds.

## 5. Conclusions

A low-power, lightweight, discrete, wearable detector system utilizing compact, high-efficiency MSND technology has been fabricated

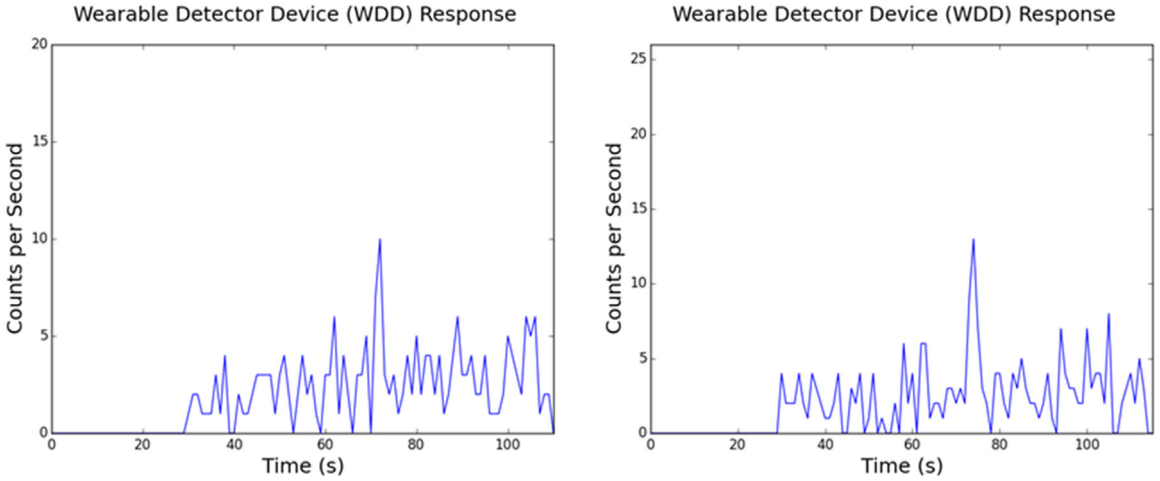


**Fig. 17.** Moving source measurements for bare $^{252}$Cf with the WDD 1 m from the source at closest approach. The source was moving at approximately 1.2 m/s in the left plot and 0.6 m/s in the plot on the right.

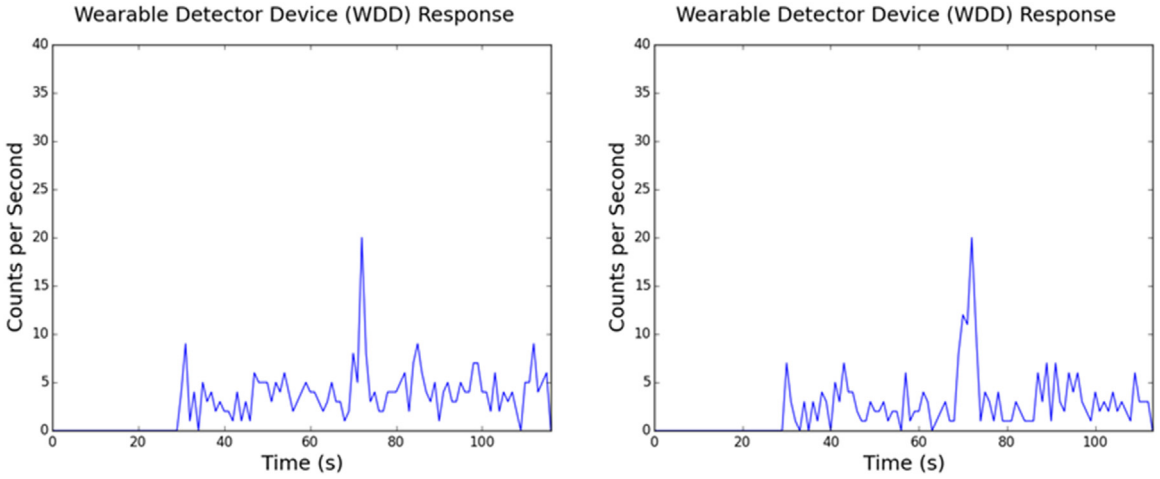


**Fig. 18.** Moving source measurements for moderated $^{252}$Cf with the WDD 1.5 m from the source at closest approach. The source was moving at approximately 1.2 m/s in the left plot and 0.6 m/s in the plot on the right.

and characterized. Sixteen MNDs, containing twenty-four, 1-cm$^2$ active-area MSNDs, connected to communications dongles, which then connect to a master control board and battery pack compose the fully populated WDD. The WDD system showed strong signal-to-background responses for bare and moderated 21.9-ng $^{252}$Cf sources and a bare AmBe source. The WDD interfaces with software on a handheld Android device for intuitive operation. The angular response showed count-rate depressions for side-on irradiation angles, but this problem may be mitigated by adjusting the MND arrangement or implementing source-direction algorithms that direct the operator to turn towards the source. Future iterations of the WDD system will likely contain Dual-Sided MSNDs (DS-MSNDs) which have significantly higher intrinsic thermal-neutron detection efficiencies (Fronk et al., 2015a, 2015b, 2014), which should improve the sensitivity of the WDD per MND in the system.

## Acknowledgements

This work was supported in part by the Defense Threat Reduction Agency, United States Contract: HDTRA1-14-C0128. Operation of the TRIGA Mk II research reactor located at Kansas State University was performed by Dr. Jeffrey A. Geuther and his reactor operations team and was greatly appreciated. Detectors were designed, fabricated, and characterized at the Semiconductor Materials and Radiological Technologies (S.M.A.R.T.) Laboratory at Kansas State University and Radiation Detection Technologies, Inc. The WDD electronics were designed and fabricated at the Electronics Design Laboratory at Kansas State University. The Android interface was designed by Alion Science and Technologies Corp.

## References

Aucott, T.J., Bandstra, M.S., Negut, V., Chivers, D.H., Cooper, R.J., Vetter, K., 2013. Routine surveys for gamma-ray background characterization. IEEE Trans. Nucl. Sci. 60, 1147–1150. https://doi.org/10.1109/TNS.2013.2251355.

Bellinger, S.L., Cooper, B.W., Fronk, R.G., Henson, L., Ochs, T., Sobering, T.J., McGregor, D.S., 2013. Characterization of microstructured semiconductor neutron detectors, In: Proceedings of IEEE Nuclear Science Symposium Conference Record. IEEE, pp. 1–7 ⟨http://dx.doi.org/10.1109/NSSMIC.2013.6829849⟩.

Fronk, R.G., Bellinger, S.L., Henson, L.C., Huddleston, D., Ochs, T.R., Smith, C.T., Sobering, T.J., Rietcheck, C.J., Taylor, R.D., Shultis, J.K., McGregor, D.S., 2014. Development of the dual-sided microstructured semiconductor neutron detector, In: Proceedings of 2014 IEEE Nuclear Science Symposium and Medical Imaging Conference (NSS/MIC). IEEE, pp. 1–4 ⟨http://dx.doi.org/10.1109/NSSMIC.2014.7431247⟩.

Fronk, R.G., Bellinger, S.L., Henson, L.C., Huddleston, D.E., Ochs, T.R., Rietcheck, C.J., Smith, C.T., Shultis, J.K., Sobering, T.J., McGregor, D.S., 2015a. Advancements on dual-sided microstructured semiconductor neutron detectors (DSMSNDs), In: Proceedings of 2015 IEEE Nuclear Science Symposium and Medical Imaging Conference (NSS/MIC). IEEE, pp. 1–4 ⟨http://dx.doi.org/10.1109/NSSMIC.2015.7582287⟩.

Fronk, R.G., Bellinger, S.L., Henson, L.C., Ochs, T.R., Smith, C.T., Kenneth Shultis, J., McGregor, D.S., 2015b. Dual-sided microstructured semiconductor neutron detectors

(DSMSNDs). Nucl. Instrum. Methods Phys. Res. Sect. A Accel. Spectrom. Detect. Assoc. Equip. 804, 201–206. https://doi.org/10.1016/j.nima.2015.09.040.

Gordon, M.S., Goldhagen, P., Rodbell, K.P., Zabel, T.H., Tang, H.H.K., Clem, J.M., Bailey, P., 2004. Measurement of the flux and energy spectrum of cosmic-ray induced neutrons on the ground. IEEE Trans. Nucl. Sci. 51, 3427–3434. https://doi.org/10.1109/TNS.2004.839134.

McGregor, D.S., Bellinger, S.L., Fronk, R.G., Henson, L., Huddleston, D., Ochs, T., Shultis, J.K., Sobering, T.J., Taylor, R.D., 2015. Development of compact high efficiency microstructured semiconductor neutron detectors. Radiat. Phys. Chem. 116, 32–37. https://doi.org/10.1016/j.radphyschem.2015.05.025.

McGregor, D.S., Bellinger, S.L., McNeil, W.J., Unruh, T.C., 2008. Micro-structured high-efficiency semiconductor neutron detectors, In: Proceedings of 2008 IEEE Nuclear Science Symposium Conference Record. IEEE, pp. 446–448 ⟨http://dx.doi.org/10.1109/NSSMIC.2008.4775204⟩.

McGregor, D.S., Bellinger, S.L., Shultis, J.K., 2013. Present status of microstructured semiconductor neutron detectors. J. Cryst. Growth 379, 99–110. https://doi.org/10.1016/j.jcrysgro.2012.10.061.

McGregor, D.S., Kenneth Shultis, J., 2011. Reporting detection efficiency for semiconductor neutron detectors: a need for a standard. Nucl. Instrum. Methods Phys. Res. Sect. A Accel. Spectrom. Detect. Assoc. Equip. 632, 167–174. https://doi.org/10.1016/j.nima.2010.12.084.

McGregor, D.S., McNeil, W.J., Bellinger, S.L., Unruh, T.C., Shultis, J.K., 2009. Microstructured semiconductor neutron detectors. Nucl. Instrum. Methods Phys. Res. Sect. A Accel. Spectrom. Detect. Assoc. Equip. 608, 125–131. https://doi.org/10.1016/j.nima.2009.06.031.

Mitchell, L.J., Phlips, B.F., Wulf, E.A., Hutcheson, A.L., Leas, B.E., 2011. Cross country background measurements with high purity germanium, In: Proceedings of 2011 IEEE Nuclear Science Symposium Conference Record. IEEE, pp. 319–323 ⟨http://dx.doi.org/10.1109/NSSMIC.2011.6154508⟩.

Nikolic, R.J., Conway, A.M., Reinhardt, C.E., Graff, R.T., Wang, TzuFang, Deo, Nirmalendu, Cheung, ChinLi, 2007. Fabrication of pillar-structured thermal neutron detectors, In: Proceedings of 2007 IEEE Nuclear Science Symposium Conference Record. IEEE, pp. 1577–1580 ⟨http://dx.doi.org/10.1109/NSSMIC.2007.4437299⟩.

Nikolić, R.J., Conway, A.M., Reinhardt, C.E., Graff, R.T., Wang, T.F., Deo, N., Cheung, C.L., 2008. 6:1 aspect ratio silicon pillar based thermal neutron detector filled with B10. Appl. Phys. Lett. 93, 133502. https://doi.org/10.1063/1.2985817.

Ochs, T.R., Bellinger, S.L., Fronk, R., Henson, L.C., Rietcheck, C.J., Sobering, T.J., Taylor, R.D., McGregor, D.S., 2014. Fabrication of present-generation microstructured semiconductor neutron detectors, In: Proceedings of 2014 IEEE Nuclear Science Symposium and Medical Imaging Conference (NSS/MIC), IEEE, pp. 1–3 ⟨http://dx.doi.org/10.1109/NSSMIC.2014.7431177⟩.

RadEyeTM NL Personal Highly Sensitive Neutron Radiation Detectors, n.d. [WWW Document] URL ⟨https://www.thermofisher.com/order/catalog/product/4250678?SID=srch-srp-4250678⟩ (Accessed 8 June 2018).

Radiation Detection Technologies, I., 2017. MSND® Tile | RDT [WWW Document]. URL ⟨http://radectech.com/products/msnd-tile⟩ (Accessed 25 July 2017).

Shultis, J.K., McGregor, D.S., 2009. Design and performance considerations for perforated semiconductor thermal-neutron detectors. Nucl. Instrum. Methods Phys. Res. Sect. A Accel. Spectrom. Detect. Assoc. Equip. 606, 608–636. https://doi.org/10.1016/j.nima.2009.02.033.

Uher, J., Fröjdh, C., Jakůbek, J., Kenney, C., Kohout, Z., Linhart, V., Parker, S., Petersson, S., Pospíšil, S., Thungström, G., 2007. Characterization of 3D thermal neutron semiconductor detectors. Nucl. Instrum. Methods Phys. Res. Sect. A Accel. Spectrom. Detect. Assoc. Equip. 576, 32–37. https://doi.org/10.1016/j.nima.2007.01.115.